



## Research paper

## Accelerated thermo-mechanical fatigue of copper metallizations studied by pulsed laser heating

Stefan Wurster<sup>a,1,2</sup>, Stephan Bigl<sup>a,\*</sup>, Megan J. Cordill<sup>b</sup>, Daniel Kiener<sup>a</sup><sup>a</sup> Department of Materials Physics, Montanuniversität Leoben, Jahnstrasse 12, 8700 Leoben, Austria<sup>b</sup> Erich Schmid Institute of Materials Science, Austrian Academy of Sciences, Jahnstrasse 12, 8700 Leoben, Austria

## ARTICLE INFO

## Article history:

Received 12 April 2016

Accepted 10 August 2016

Available online 20 August 2016

## Keywords:

Copper metallization

Thermo-mechanical fatigue

Microstructure

Laser heating

Electron backscatter diffraction

Atomic force microscopy

## ABSTRACT

Fatigue is an important reliability issue for microelectronics. In this work, a technique for fast thermal cycling of thin films on substrates is introduced using an infrared laser beam. The advantages of this method are the significantly increased heating and cooling rates compared to conventional slow furnace processes, and the use of readily available small pieces of metallized wafers, which avoid complicated sample preparation. To demonstrate the applicability of the new experimental setup two copper metallization films, differing in their content of additives used for film deposition, on silicon substrates were investigated with respect to microstructural, topographical and electrical changes due to pulsed thermo-mechanical loading. The results, such as grain growth and roughness evolution, are compared to results from specimens which experienced slow infrared furnace cycling. Furthermore, changes in electrical sheet resistance are shown. When analyzing the outcomes from processes of different heating/cooling rates, it can be stated that accelerated laser heating leads to faster changes in these properties which enables fast screening of metallization materials under development.

© 2016 Elsevier B.V. All rights reserved.

## 1. Introduction

During switching operations temperatures in semiconductor devices rise substantially. As these devices are composed of a stack of different materials, having differences in elastic (Young's Modulus), plastic (yield strength) and thermal (coefficient of thermal expansion, CTE) properties, stresses evolve. Repeated switching, i.e. repeated cycles of heating and cooling, leads to changes of the film microstructure. The driving force for this phenomenon, besides diffusional processes at elevated temperatures, is the existence of stresses within the layered material. Considering a two material system, such as a thin copper layer on a thick silicon substrate, these stresses originate from differences in the CTEs leading to biaxial compressive or tensile stress states. The CTE for silicon is between  $\sim 3.45$  ppm/°C for 170 °C and  $\sim 3.97$  ppm/°C for 400 °C [1], whereas the CTE-values for polycrystalline copper are between  $\sim 17.9$  ppm/°C and  $\sim 19.3$  ppm/°C [2] at the same temperatures. In other words, heating of the specimen leads to compressive stresses in the faster expanding metallization layer, while tensile stress states prevail at low temperatures [3–5]. The combined effects of temperature

(diffusion) and stresses might be grain growth, surface roughening and texture changes [5,6]. Texture changes can originate from rotations of the crystals or growth of preferentially oriented grains. Thus, microstructural and topographical changes are very likely to be observed due to thermal cycling. In a progressed state of thermo-mechanical cycling, voids can nucleate [5] or cracks might form, thereby degrading the mechanical and electrical properties and limiting the operational life-time. Thus, the investigation of thermo-mechanical fatigue and the integrity of metallization layers is a key issue regarding reliability of semiconductor devices.

Copper, being one of the main materials for metallizations in semiconductor technology due to its outstanding thermal and electrical properties, was chosen as the material to be subjected to thermo-mechanical cycling. To achieve thicknesses of several micrometers commonly used for metallization layers, electrochemical deposition was applied for the material used in this study. With the usage of electro-deposited materials comes the freedom of process parameters and the usage of different additives leading to differently microstructured films having the desired properties. In this publication, changes and similarities in the fatigue behavior of two films containing different amounts of inorganic residuals, originating from the deposition process is one of the topics that will be addressed.

For thermal cycling of materials, a variety of experimental procedures are available. Usage of the wafer curvature technique offers the possibility to directly determine the evolving stresses [4,7,8]. However, the heating and cooling rates are very low, which lies in the range of

\* Corresponding author.

E-mail address: [stephan-paul.bigl@stud.unileoben.ac.at](mailto:stephan-paul.bigl@stud.unileoben.ac.at) (S. Bigl).<sup>1</sup> Both authors contributed equally to this work.<sup>2</sup> Present address: OTTRONIC Technology Laboratory, OTTRONIC GmbH Austria, Villenstrasse 10, 8740 Zeltweg, Austria.

0.17 °C/s. Slightly accelerated heating and cooling is offered by infrared furnaces [3,5], which was used for previous works on equivalent materials [4,5]. With conventional heating techniques, it is difficult to achieve high cycle numbers (e.g. > 10<sup>5</sup> cycles). When it comes to a fast screening of thermo-mechanical fatigue behavior of new materials and stack-designs, a method that i) uses easily available cut pieces of metallized wafers that did not undergo any further processing towards the device level and ii) has a high repetition rate is desirable. These requirements are fulfilled by the laser-driven thermo-mechanical cycling technique introduced in this work.

## 2. Materials and experimental methods

### 2.1. Laser setup

The proposed accelerated thermal cycling method uses an infrared laser (LM250 diode laser, passively water cooled, company: Dr. Mergenthaler GmbH & Co KG, Neu-Ulm, Germany). It operates in the near infrared regime at a wavelength of 940 nm. The experimental setup relies on a laser beam hitting the silicon surface, heating the silicon and in an indirect way through heat conduction, heating the metallization layer. Silicon has a certain transmissivity at 940 nm [9], thus, adequate parts of the substrate volume and not only the surface near region are heated during a short laser pulse (~0.25 s). The copper film temperature is measured in a contact-free way via a pyrometer pointing at the metallized surface. The pyrometer points to the exact opposite site of the specimen (front side), where the laser beam hits the silicon backside. One representative thermal cycle, defined by laser output power, measured temperature and the resultant heating/cooling rate is presented in Fig. 1. To avoid any effects from the running-in period of the laser process, the single cycle was taken from a later stage of the cycling process. To gain the possibility to operate in vacuum or any desired inert atmosphere, the specimen is positioned within a vacuum chamber.

The laser optics collimating the laser beam, exiting from the light conducting cable are positioned within a housing for safety reasons. A similar safety housing is available for the pyrometer, positioned outside of the vacuum chamber. The laser beam enters into the vacuum chamber through a special vacuum-sealed window which reduces reflection and optimizes transmission of the desired wavelength. Using a silver mirror within the vacuum chamber, the laser light is deflected by ~90°. The specimen is positioned within a dedicated specimen holder without fixation, since any fixation would interfere with the intrinsic

specimen deformation and would lead to fracture of the expanding and bowing sample during thermal cycling.

An important experimental detail is that, for programming the laser power cycles via the measured temperature, not the desired temperature of 400 °C but a lower temperature has to be used. As the laser beam irradiates the backside of the specimen, the heat generated in the backside near region has to be conducted through the substrate and metallization layer to the upper metallized surface. This is the place where the temperature is measured with the calibrated pyrometer. The time needed for heat conduction leads to a delay in the measured temperature signal compared to the set temperature as well as to the defined laser power pulse, as it is shown in Fig. 1. Thus, depending on the thickness of the used specimen and its heat conductivity, the set temperature must not be set to the desired temperature, but to a lower value.

To prevent the metallization layer from oxidation, as it would be the case for copper at elevated temperatures, the vacuum chamber is first evacuated using a membrane pump to a pressure of approximately 3 mbar and then carefully vented again to a pressure of ~160 mbar using forming gas composed of N<sub>2</sub>/H<sub>2</sub> with 95 vol.% N<sub>2</sub>. Furthermore, forming gas provides active cooling through convection.

The slow furnace process [5] had a maximum heating rate of 17 °C/s and the maximum cooling rate was -3 °C/s. With the new experimental setup, this value is considerably increased to a maximum heating rate of 1450 °C/s and a maximum cooling rate of -280 °C/s (blue dotted line in Fig. 1). Comparing furnace and laser cycling, the heating rate and, thus, the strain rate are increased by two orders of magnitude. Hence, the time for diffusional processes is considerably smaller.

To bridge the gap between infrared furnace cycling and fast laser cycling experiments, thermal cycling was performed at a low pressure of approximately 3 mbar forming gas atmosphere. This led to cycle times of about 9 s, which is 10 times faster in comparison to infrared furnace cycles (~95 s) but three times slower compared to fast laser cycling using forming gas cooling at a pressure of 160 mbar. Despite careful experimental control, an evolution of surface oxides cannot be completely suppressed. Thus, the specimens were put into 100 vol.% acetic acid for 3 min at a temperature of 35–40 °C. This procedure does not affect the copper surface [10] and has already proven very useful [5,11].

### 2.2. Metallization systems

For the investigation of the thermo-mechanical fatigue behavior resulting from fast laser heating and the comparison to slow furnace heating performed in [5], 5 μm thick electrochemically deposited polycrystalline copper films on 725 μm thick silicon wafers of (100)-orientation were used. Copper was deposited on a thin layer of a tungsten-based diffusion barrier, which can be seen as a bright region between copper and silicon in the cross-sectional micrographs. After electrodeposition, annealing for half an hour was performed at 400 °C in an inert atmosphere, which guarantees stable microstructures at room temperature.

Two different copper metallizations were used for this study. One film system, Film A, was designed with a high amount of additives, whereas the second customized material, Film B, was deposited using significantly less inorganic additives and can be regarded as a pure copper film. Details on the chemical composition of both films can be found in Wimmer et al. [12]. The occurring changes during comparatively slow thermal cycles have extensively been discussed in a previous publication [5], where restricted microstructural changes in Film A can be attributed to the presence of incorporated inorganic residual elements. Furthermore, the films were designed in a way to show identical starting microstructures, as will be shown in a forthcoming section. Insignificantly small differences in grain size (Fig. 3a), texture or twin occurrence rule out these starting parameters to influence the outcome of thermo-mechanical fatigue experiments. Besides the

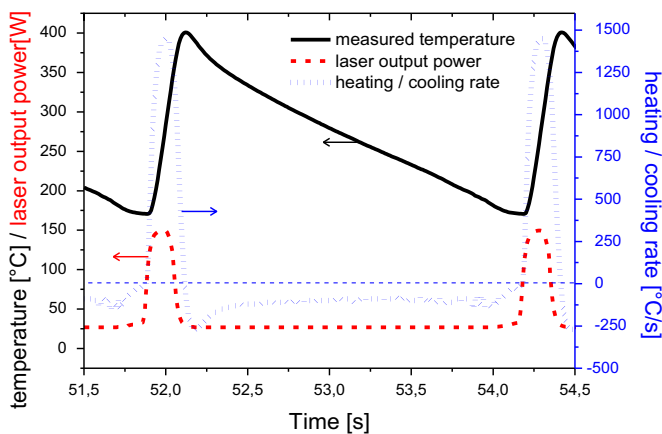


Fig. 1. A representative heating/cooling cycle showing the pyrometer-measured temperature (continuous black line), the used laser power (dashed red line) as well as the achieved heating and cooling rates (dotted blue line).

difference in content of inorganic elements, Film B is slightly rougher than Film A (Fig. 3b).

### 2.3. Experimental methods

To monitor microstructural and topographical changes, a tracking method, proposed by the authors in [11] was used. It is possible to observe the same site throughout the complete thermal cycling process. This tracking relies on marking a representative large area with small Vickers microindents, using a force of 20 gf or 50 gf. These indents can easily be found using a scanning electron microscope (SEM) or an atomic force microscope (AFM).

Keeping some distance from the indents in order not to incorporate the plastically deformed regions close to them into the investigation, an area of at least  $120 \times 120 \mu\text{m}^2$  was scanned with a constant step size of  $0.2 \mu\text{m}$  with Electron Backscatter Diffraction (EBSD, EDAX Digiview Camera in combination with TSL Data Collection and TSL Analysis software, version 5). The EBSD system is attached to a SEM of type LEO 1525 (Zeiss, Oberkochen, Germany). For the definition of a grain to determine the mean grain size, a maximum tolerance angle of  $15^\circ$  and a minimum grain size of 3 pixels was allowed. The Inverse Pole Figure (IPF) maps overlaid with the image quality (IQ), were processed using a confidence index clean up with a threshold value of 0.07.

In addition, an area of  $50 \times 50 \mu\text{m}^2$  was scanned using an AFM (Bruker Inc., Billerica, USA), where the AFM-scanned area is incorporated within the EBSD-scanned area. AFM height images have a scan resolution of 512 lines and were post-processed using Gwyddion 2.36 software [13]. With EBSD and AFM data at hand, it is possible to track microstructural (grain size and texture) and topographical (roughness) changes of the same area throughout the whole experiment. To reveal microstructural changes underneath the surface, film cross-sections were made with a dual beam Focused Ion Beam (FIB) workstation (Auriga SEM/FIB, Zeiss, Oberkochen, Germany). For cutting rough trenches, a gallium ion beam of 5 nA was used. Fine polishing was performed with a lower current of 200 pA. No deposition of heavy elements on top of the region of interest by a gas injection system was used.

To determine changes in the electrical resistivity of the material, the sheet resistance of the as-received and thermo-mechanically cycled thin metallic films was measured with a collinear four-probe array, as described in ASTM F390 [14]. The experimental setup consisted of a Keithley 2400 sourcemeter supplying a constant current of 50 mA, a Keithley 2182 nanovoltmeter and a Cascade C4S four probe array. Omitting discrepancies between different specimens (such as the exact specimen size and shape, slight differences in metallization thickness), a tracking method was again used. The specimens of Film A and Film B, used for resistivity measurements after 0, 250 and 1000 cycles, were the same specimens only cleaned with acetic acid prior to measurements; then cycled again. The film thickness, a quantity needed for calculating the resistivity, was determined from FIB cross-sections of the starting material. The additional layer of metallic tungsten-based diffusion barrier was not taken into account. This decision was made because of its low thickness ( $\sim 5\%$  of the copper layer) and its high resistivity ( $\sim 3$  times the resistivity of copper), leading to a constant total contribution of  $\sim 1\%$  to film conductivity. The resistivity  $\rho$  was calculated via the sheet resistance  $R_\square$  and the film thickness  $d$  according to Eq. (1)

$$\rho = d * R_\square = d * R_{avg} * c * F * F_{sp}. \quad (1)$$

To calculate the sheet resistance  $R_\square$  from the average specimen resistances  $R_{avg}$ , correction factors,  $c$ , taking into account the lateral dimensions of the specimen,  $F$ , comparing the film thickness ( $5.1 \mu\text{m}$ ) with the probe distance (1 mm) and  $F_{sp}$ , considering the probe spacing, are needed. Due to the thin film in relation to the thick substrate  $F$  can be set to 1. More details on the correction factors can be found in [14].

## 3. Results

### 3.1. Initial metallization microstructures

Fig. 2 shows the initial microstructures of Film A and Film B presented as IPF maps with cross-sections of the film and scanning electron micrographs of the surface. The standard triangle shown is the color code for reading the IPF maps and is valid for all presented maps. The slight (111)-texture of both films (see Fig. 4a for Film B,  $N = 0$ ) becomes evident through a slight surplus of blue colored grains. To emphasize the grain structure, high angle grain boundaries (HAGB) with orientation changes larger than  $15^\circ$  are represented by white lines and  $\Sigma 3$  twin boundaries, HAGB having orientation changes between  $59^\circ$  and  $61^\circ$  to be precise, are shown as black lines. Both materials reveal a polycrystalline, slightly textured microstructure with a high amount of twin boundaries. The area weighted twin boundary length is  $\sim 1 \mu\text{m}/\mu\text{m}^2$ , whereas the area weighted HAGB length is  $\sim 0.5 \mu\text{m}/\mu\text{m}^2$  for both materials. The average initial grain size is identical for all three tracked regions (see Fig. 3a) and ranges between  $3.2 \mu\text{m} \pm 1.0 \mu\text{m}$  and  $3.4 \mu\text{m} \pm 1.1 \mu\text{m}$  for Film A and Film B, respectively. The determination of the grain size distribution and the mean grain size does not take into account the  $\Sigma 3$  twin boundary as a special coincidence site lattice boundary but as any arbitrary HAGB. The grain size would increase when removing  $\Sigma$ -boundaries from the calculations and only considering randomly oriented HAGBs.

The measured resistivities of  $1.81 \times 10^{-8} \Omega\text{m}$  (Film A, higher inorganic element content) and  $1.77 \times 10^{-8} \Omega\text{m}$  (Film B, pure copper) in the non-cycled state are in good accordance to the reference value of  $1.68 \times 10^{-8} \Omega\text{m}$  (pure bulk Cu at 293 K [15]). The root-mean-squared (RMS) roughness of the metallization, measured within the tracking area, is as follows: 34 nm for Film A and 88 nm and 82 nm for the tracking regions of Film B, used for investigations of fast and slow thermal cycling. Comparing the left and right side of Fig. 2 and from the data given above, it can be stated that both films are, besides a slightly smoother surface of Film A, very similar in their microstructural and electrical properties.

### 3.2. Change of global parameters during thermo-mechanical cycling

With regard to thermo-mechanical cycling, the evolution of global film parameters such as grain size, strength of texture, resistivity and roughness are presented in this section. The grain size, an easily accessible parameter via EBSD-results, shows an increase for all three investigated specimens (Fig. 3a). The increase in grain size for Film B is larger than for Film A. When only considering Film B, the fast cycling led to an increase in grain size from  $3.4 \mu\text{m} \pm 1.1 \mu\text{m}$  to  $9.4 \mu\text{m} \pm 2.5 \mu\text{m}$  after 1000 cycles, whereas the slow cycling changed the grain size from  $3.3 \mu\text{m} \pm 1.1 \mu\text{m}$  to  $5.7 \mu\text{m} \pm 1.7 \mu\text{m}$ . The increase in grain size for Film A (only fast laser cycling data available) is less compared to the slow thermal cycling of Film B. There is a small increase from  $3.2 \mu\text{m} \pm 1.0 \mu\text{m}$  to  $5.2 \mu\text{m} \pm 1.8 \mu\text{m}$  after 1000 cycles.

The evolution of roughness is quantified by using the RMS roughness (Fig. 3b). The roughness of Film A, which is smoother in the initial stage, catches up after about 250 cycles, and the further increase in roughness is very similar to Film B. After 1000 cycles, the three films reach RMS roughness values between 320 nm and 368 nm. With respect to the initial RMS roughness, the roughness of Film A increases by a factor of 10, and the RMS roughness of Film B only increases four times.

By taking the likelihood of the appearance of (100)-oriented grains from the IPFs (Fig. 4 and similar data for the remaining two specimens), it is possible to derive Fig. 3c. A significant increase in the (100)-texture intensity for Film B (fast cycling) can be observed, while the slow process applied to Film B exhibits a less pronounced increase. Film A revealed a marginal increase in (100)-texture. This confirms earlier work [5], where it was shown that Film B, subjected to identical thermal cycling as Film A, changes its texture faster than Film A.

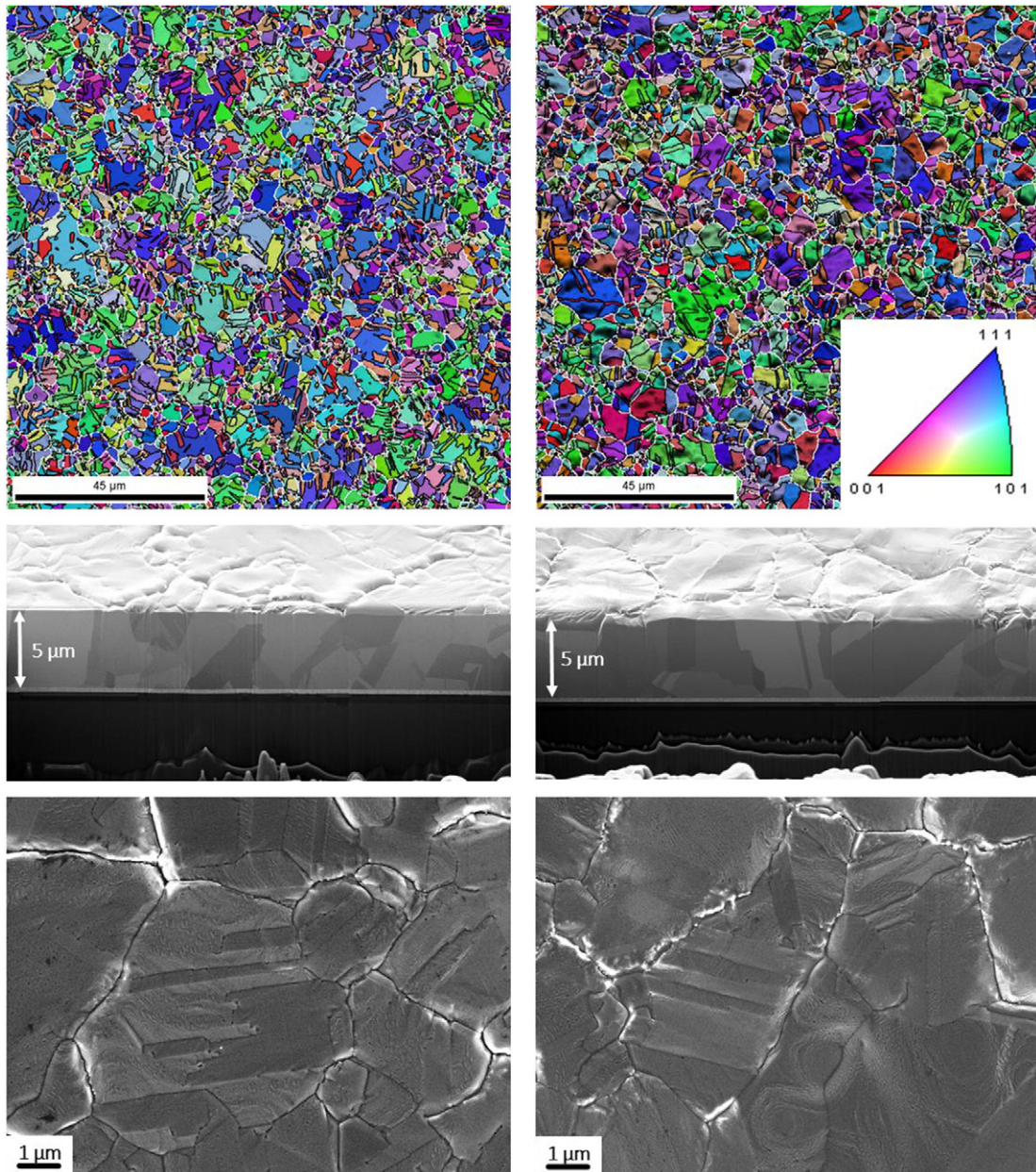


**Fig. 2.** Initial microstructures of Film A (left column) and Film B (right column). The IPFs (first row), FIB cross-sections (second row) and scanning electron micrographs (third row) of both materials demonstrate the almost identical starting microstructure with similar grain sizes, twin occurrence, texture and film thickness. HAGB are added to the IPF maps. The standard triangle, needed for reading the IPFs, applies for all figures in this publication. Contrast and brightness of scanning electron micrographs were altered for better visibility of microstructural features.

To demonstrate the texture evolution of the metallization, the IPFs are presented in Fig. 4, where the increasing strength of the (100)-poles with cycle number is clearly visible. From a qualitative point of view, there is a change of the appearance of IPF maps, especially for the pure material Film B, when comparing Fig. 6a with Fig. 6e. A typical example, which is in coincidence with the IPFs of Fig. 4, is the (111)-oriented, blue grain in the upper left corner of Fig. 6a containing several twins. The most prominent twin is a (100)-oriented, red region within the center of the grain. Both processes, a growth of the whole grain, as well as an increase of the size of the twinned, red region take place. In total, the red colored area is growing substantially, which is represented in the sequence of Fig. 4.

With increasing number of thermo-mechanical cycles, there is an increase in roughness and the formation of voids may also occur [5]. Both roughness and voids could lead to an increase in electrical resistivity  $\rho$  of the material. For the resistivity investigation, again, a tracking technique

was used and the diagram shown in Fig. 3d was generated from single specimens of each material using the fast cycling process. Normalized to the resistivity of the non-cycled state,  $\rho_0$ , the increase in resistivity  $\rho$  is identical for both films and reaches approximately 1.1  $\rho_0$  after 1000 cycles.

### 3.3. Local microstructural evolution during thermo-mechanical cycling

As already shown in Fig. 3, both film systems undergo significant changes of their microstructure. For a detailed mechanism-based description of these changes, Figs. 5 and 6 reveal crystallographic and topographical changes of Film A and Film B throughout the whole process. In both cases the same surface sections are shown after 0, 100 and 1000 cycles. For the ease of illustration, only twin boundaries are indicated in the IPF-IQ images for 1000 cycles (Figs. 5e, 6e).

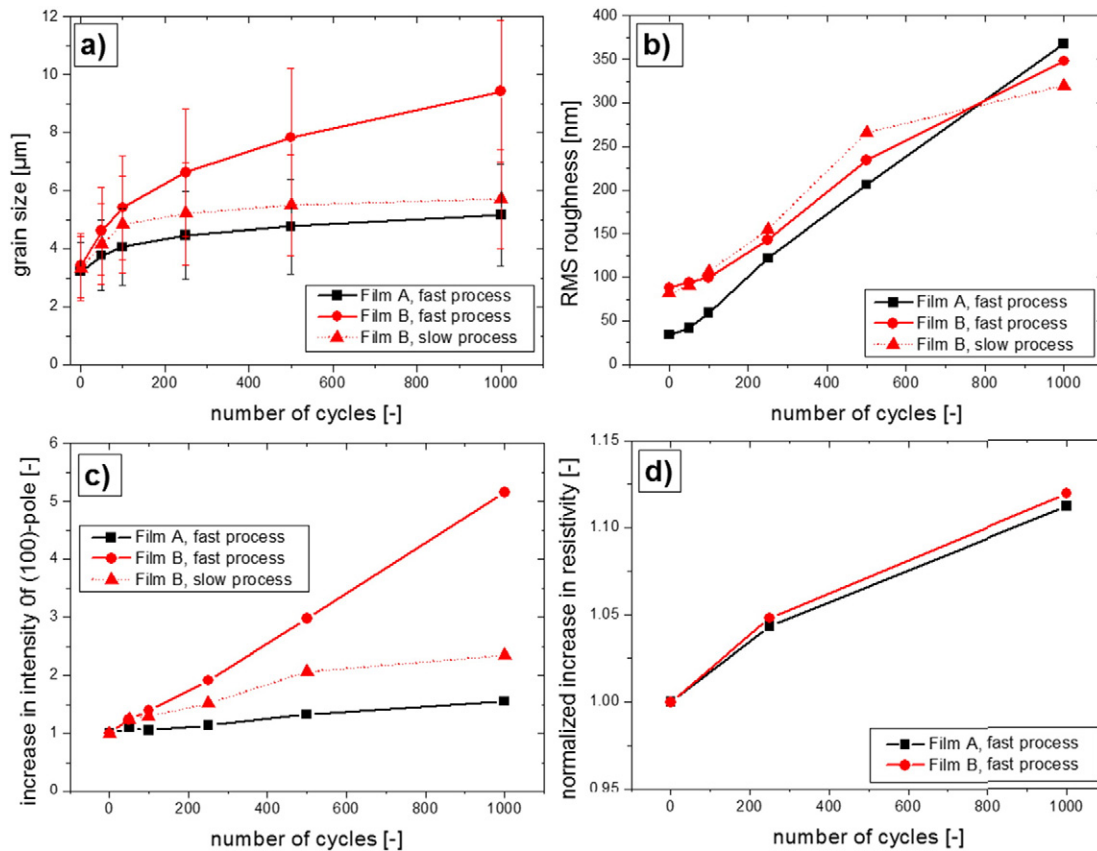


**Fig. 3.** Change in global parameters grain size, surface roughness, texture and resistivity with increasing number of thermo-mechanical cycles. Both films were subjected to fast thermal cycling. Film B was also subjected to a slower process. a) Grain size calculated from EBSD scans. The mean grain size value and the standard deviation of a log-normal grain size distribution are shown. b) Increase in RMS roughness measured with AFM. The roughness was determined on identical regions in tracking mode. c) Change in intensity of the (100)-pole in the IPFs (see Fig. 4), normalized to the intensity of the non-cycled state. The texture changes faster the higher the heating/cooling rates. While the texture of Film A almost stays constant, there is a pronounced change for the fast cycled Film B. d) Increase in resistivity of Film A and Film B with increasing number of cycles, normalized to the initial resistivity of the non-cycled specimen. No specimen that experienced the slow laser-based thermal cycling was included in this investigation.

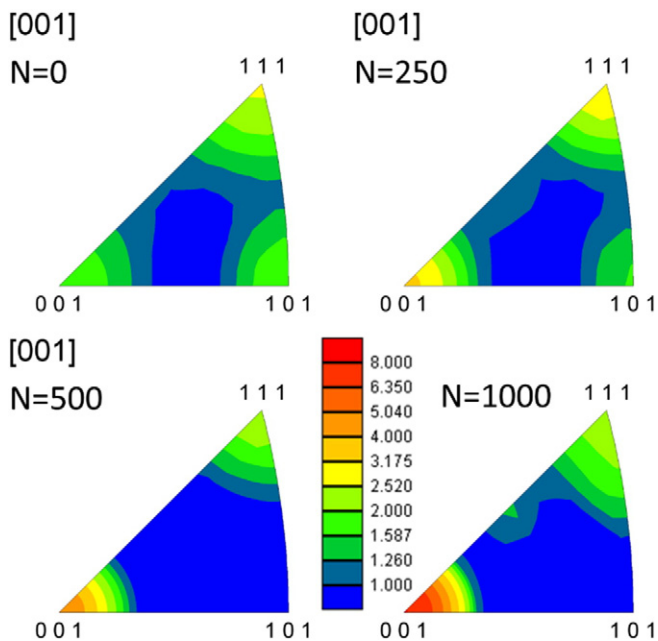


**Fig. 4.** IPFs for Film B, fast cycling mode. Only identified grains were allowed to contribute to the texture evolution. The change in texture from a slight (111)-texture for the initial state to a pronounced (100)-texture after 1000 cycles is evident. The color shows the likelihood of appearance of certain crystal orientations compared to a random orientation (=1, border blue/dark blue). The color code applies to all four IPFs in the figure.

The film system with the higher inorganic element concentration, Film A, exhibits an initially non-textured microstructure (Fig. 5a,b) with a dense network of twins with different twin-parent configurations within a grain. Initial cycling led to slight grain growth (Fig. 5c,d), whereas further cycling up to 1000 cycles (Fig. 5e,f) resulted in severe roughening at grain boundaries as well as faceting of shear band like fatigue structures between twin-configurations. After 1000 cycles, the fraction of twin boundaries is significantly reduced compared to the as received state. Furthermore, it appears that certain grains undergo rotation throughout cycling, and therefore change their color in the IPF maps (Fig. 5a,c,e). To highlight the most notable changes, three microstructural features are highlighted in the graphs. Feature 1 indicates normal grain growth between 0 and 100 cycles of a twinned grain. From the AFM images (Fig. 5b,d) it can be seen that the original HAGB groove from the initial microstructure (Fig. 5b) still exists, even though grain growth occurred. Feature 2 highlights the evolution of a shearband-like faceting of a twinned grain between 100 and 1000 cycles. Finally, grain rotation is indicated by Feature 3 where it can be seen that the color changes throughout the cycling.

Fig. 6 illustrates microstructural changes with respect to thermo-mechanical cycling of Film B. The initial microstructure (Fig. 6a) comprises of a randomly oriented network of grains and a wavy surface topography (Fig. 6b). Upon cycling, significant grain growth can be observed, even in the early stage (Fig. 6c). Further cycling led to severe roughening, indicated by faceting between grains and certain twin-parent configurations, and an overall reduction of twin boundary length. As also seen for Film A, initial cycling for Film B, did not lead to a severe change in roughness, even though pronounced grain growth was

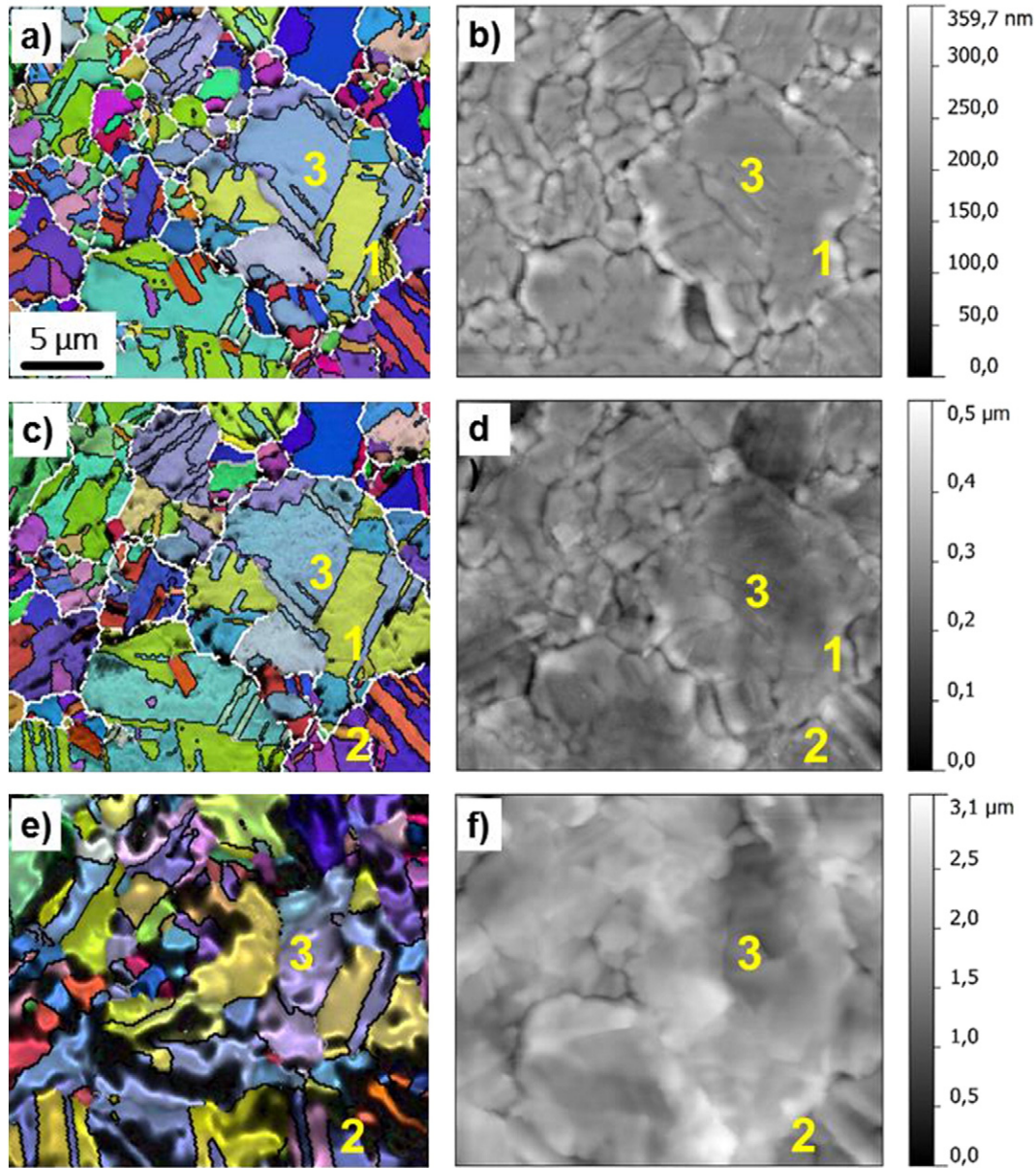


**Fig. 5.** Site specific microstructural evolution of Film A. Crystallographic evolution (a, c, e) is matched with the topographical evolution (b, d, f) of the same surface area for 0, 100 and 1000 cycles. Additionally, three distinct features (1, 2, 3) described in the text highlight microstructural changes.

found after the first 100 cycles. The subsequent cycling led then to severe roughening. To point out dominant microstructural mechanisms, three distinct features are marked. Feature 1 represents the significant growth of a (100)/(212) parent/twin grain due to thermal cycling. This preferred growth illustrates the strong texture intensity increase of the (100) out-of-plane orientation, which can be seen in Fig. 3c. This coincides with a shrinkage of (110) oriented grains and its twins, indicated by Feature 2. This texture evolution is in agreement with Fig. 4, which shows the corresponding IPFs. Feature 3 presents pronounced grain growth in the first 100 thermal cycles. The large (111) oriented grain (Fig. 6c) had emerged at a site with initially randomly oriented smaller grains (Fig. 6a). When looking at the topographical changes, it becomes obvious that these crystallographic changes are not necessarily linked to the topographical evolution. After 100 cycles (Fig. 6d) one can see still the distinct grooves of the small grains, which are also present in the initial stage (Fig. 6b).

#### 4. Discussion

When summarizing the results from the previous section, it becomes evident that distinct differences in the thermo-mechanical fatigue behavior between Film A and Film B are present. The main differences can be addressed to grain growth, texture evolution and potential void formation.

Compared to the initial state, the grain size of Film A increases by about 60%, while Film B showed a larger increase in grain size of about 176% compared to the grain size in the as-received state. This follows the significant increase of the (100)-texture component, as will be discussed later. The presence of inorganic species in the ppm range (mostly chlorine and sulphur) in Film A are the reason for the stable microstructure, whereas the distinctively lower inorganic residual concentration of Film B leads to higher grain boundary mobility and grain growth.

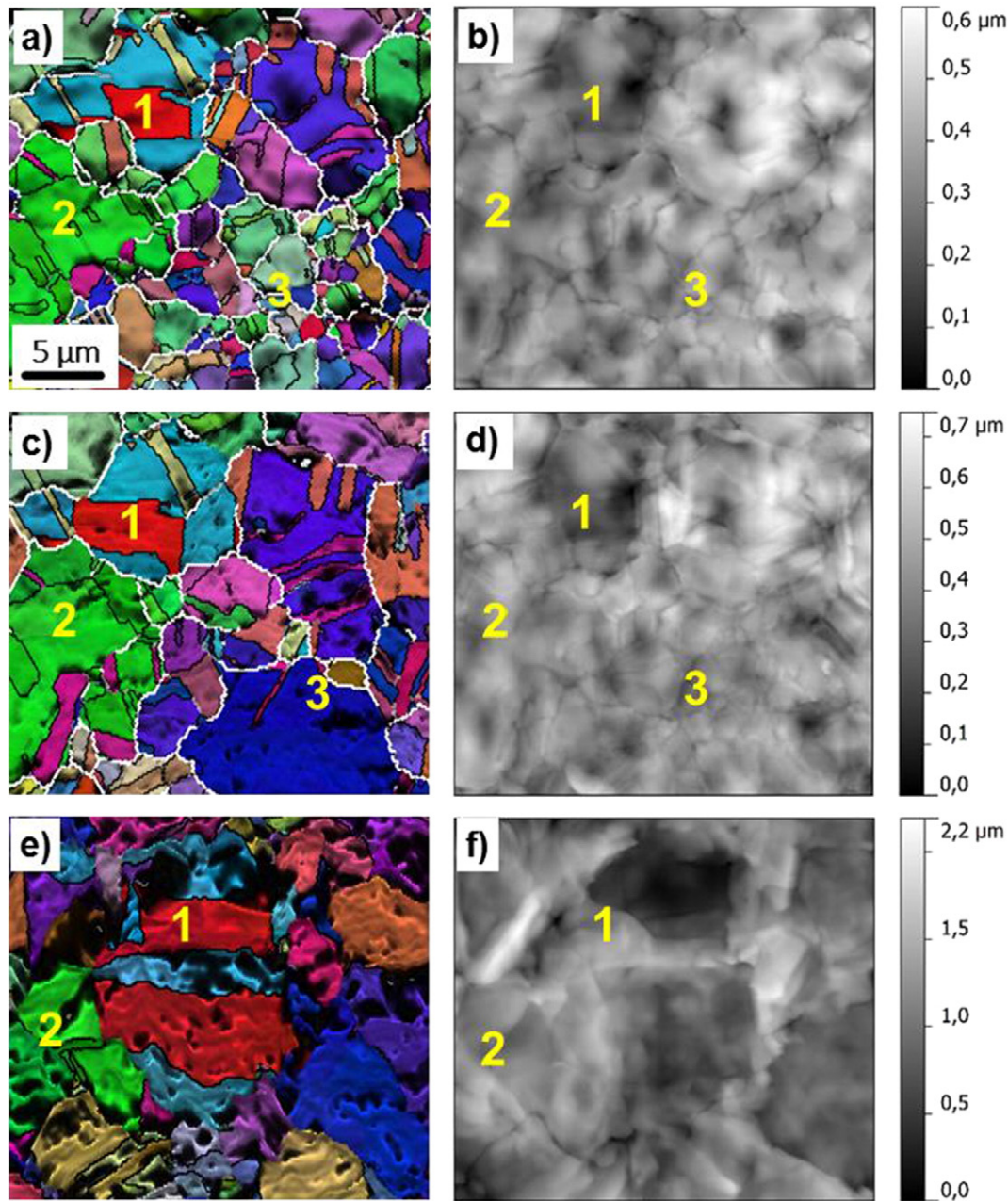


**Fig. 6.** Site specific investigations of Film B. Crystallographic evolution (a, c, e) is matched by the topographical evolution (b, d, f) of the same surface area for 0, 100 and 1000 cycles. Three distinct features (1, 2, 3) highlight microstructural changes described in the text.

Regarding the resistivity/sheet resistance, both film types show a very similar trend in increasing resistivity. Starting from about the same value of resistivity ( $\sim 1.8 \times 10^{-8} \Omega\text{m}$  for both films), the values increase by about 10% after 1000 cycles. When comparing the FIB cross-sections of both films (Fig. 7a and b), voids formed in Film A but do not seem to influence the resistivity. However, the identical behavior in increasing resistivity matches very well to the increase in absolute values of RMS roughness, where both films again show the same behavior with an approximately linear increase from below 100 nm (0 cycles) to above 300 nm (1000 cycles). Fig. 7c and d show micrographs of the surface of cycled specimens emphasizing the similar roughness evolution. For a further discussion, the sheet resistance  $R_{\square}$  shall be used instead of resistivity  $\rho$ , as the determined resistivity becomes dependent on extrinsic film properties such as the changing film thickness and voids within the material. It does not represent an intrinsic material property anymore. Assuming a small number of additional vacancies

and dislocations after thermal cycling, a constant copper resistivity  $\rho_{\text{Cu}}$  throughout the whole cycling process can be used. Thus, the increase in sheet resistance comes from a changing morphology of the films with the contribution of roughness being more dominant than the contribution of the voids. It seems that the electric current can bypass small, globular or columnar voids easily without a significant increase in the current pathway, whereas the long-range changes in surface topography, and thus film thickness, are responsible for the resistivity increase. An increasing value of RMS roughness can also be seen as a wider spread of the film thickness distribution that leads to a higher sheet resistance, which scales with  $1/d$ . In other words, a serial connection of two identical resistors, with their resistance being defined by their thickness  $d$ , would increase its total resistance when changing the thicknesses of both resistors to  $d + \Delta d$  and  $d - \Delta d$ .

Comparing the results of the development of grain size and roughness with results described in [5] one can judge that the higher

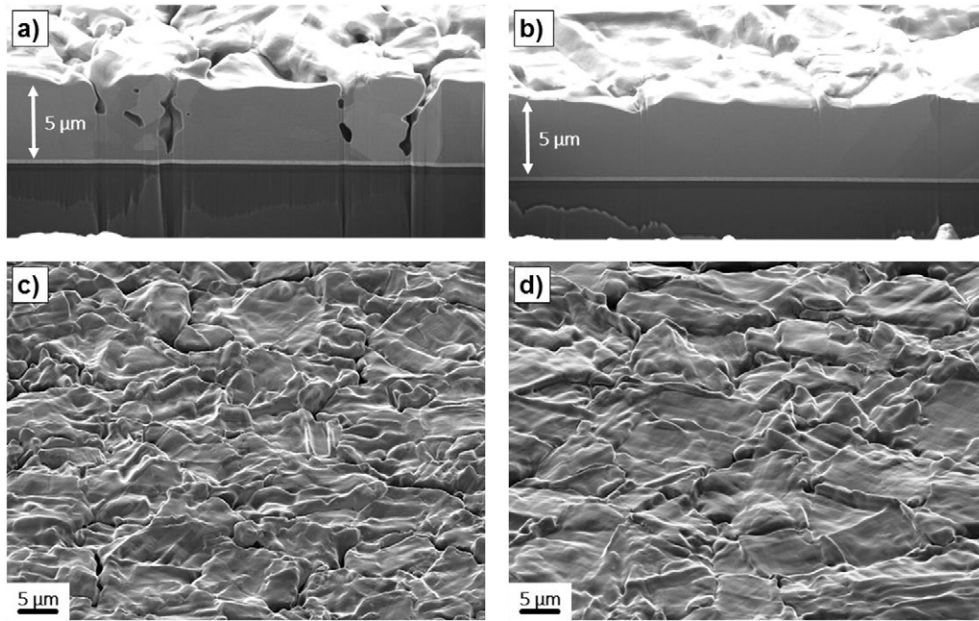


**Fig. 7.** SEM images of FIB-made cross-sections (top row) and the surface (bottom row) and of Film A (left column) and Film B (right column). The micrographs of the surfaces were taken at an inclination of 54°, also used for FIB-cutting, emphasizing the roughness evolution of the films. Although the roughness evolution of both films is very similar (see Fig. 3b), the difference becomes evident in the cross-sections. Voids formed during thermo-mechanical cycling in Film A. Contrast and brightness were altered for better visibility of microstructural features.

heating/cooling rates, and thus the externally applied strain rate, led to a faster increase in roughness and grain size. For Film B, the infrared cycling with the same temperature range (170 °C–400 °C) led to a grain size of  $5.3 \mu\text{m} \pm 1.8 \mu\text{m}$  after 1000 cycles. When using the fast laser cycling mode, however, the increase in grain size is significantly larger after the same number of cycles ( $9.4 \mu\text{m} \pm 2.5 \mu\text{m}$ ). Such accelerated grain growth can also be found for Film A. Here, slow infrared cycling increased the grain size by a small amount from  $2.8 \mu\text{m} \pm 0.9 \mu\text{m}$  to  $3.5 \mu\text{m} \pm 1.1 \mu\text{m}$  after 1000 cycles, whereas fast laser cycling increased the grain size from  $3.2 \mu\text{m} \pm 1.0 \mu\text{m}$  to  $5.2 \mu\text{m} \pm 1.8 \mu\text{m}$  after 1000 cycles.

The same trend holds true for RMS roughness values, where the increase is faster for laser cycling in comparison to slow testing. For slow furnace cycling, the roughness values only changed from about the same starting values to 100 nm (Film A) and 150 nm (Film B) after 1000 cycles. Laser cycling led to higher RMS roughness values between 320 nm and 368 nm, respectively.

Based on works of Flinn et al. [16] and Ashby et al. [17], these amplified changes in grain growth and roughness at higher strain rates might be attributed to the critical stress required for dislocations to surpass obstacles of a free energy  $\Delta F$ . This critical stress at the transition from linear elastic behavior to stress relaxation in a stress vs. temperature diagram is given by Eq. (2)

$$\sigma = \tau \left\{ 1 - \left[ \frac{kT}{\Delta F * \ln(\dot{\epsilon}_p/\dot{\epsilon}_0)} \right] \right\}, \quad (2)$$

with  $\tau$  being the stress that is required to reduce the effective height of the obstacle to zero,  $k$  being the Boltzmann constant,  $T$  the temperature,  $\dot{\epsilon}_0$  a characteristic constant and  $\dot{\epsilon}_p$  the plastic strain rate. Although the dependence of stress on strain rate is logarithmically weak, the occurrence of plastic behavior is, nevertheless, a function of the heating and cooling rate. The higher stresses for higher strain rates could lead to stress driven grain boundary migration, whereas the limited time for diffusional processes could hinder the surface from being smoothed after dislocation activity had generated a rough surface.

The statement that higher stresses develop during faster cycling is supported by experimental results of the (100)-texture evolution. A preferable growth of the (100) out-of-plane orientation made it five

times more likely after 1000 cycles for Film B. For the slow infrared cycling, the appearance of the (100)-texture component was increasing only by a factor of about 1.45 after 1000 cycles for Film B [5]. The reason for the preferential growth of the (100)-component is that the amount of applied total strain is externally defined by the difference between the coefficients of thermal expansion. For copper, the (100) texture minimizes the elastic strain energy density since it has the lowest biaxial modulus [18], thus, the difference in elastic strain energy density can be seen as the driving force for preferable (100) texture evolution. An example for the difference in strain energy  $\Delta W_\varepsilon$  for the fully plastic case is given by

$$\Delta W_\varepsilon = \frac{\sigma_{111}^2}{M_{111}} - \frac{\sigma_{100}^2}{M_{100}}, \quad (3)$$

where  $\sigma_{111}$  and  $\sigma_{100}$  are the arising stresses in the particularly oriented grains with the corresponding biaxial moduli  $M_{111}$  (261 GPa [19]) and  $M_{100}$  (115 GPa [19]). The example uses (111) and (100)-oriented grains, since they have the largest difference in the biaxial modulus. From Eq. (3) it becomes evident that the driving force and, hence, the accelerated texture evolution are strongly dependent on the resulting stresses within the grains. In both experimental cases (infrared furnace, laser heating device), the temperature change was between 170 °C and 400 °C, thus, there was no difference in the total applied strain. Therefore, it seems that for the laser cycling the elastic regime becomes larger, resulting in larger stresses and a higher driving force  $\Delta W_\varepsilon$ .

The question of whether this behavior holds true for even shorter heating/cooling pulses, e.g. in the milliseconds range or below, as they are achieved in real devices, cannot be answered within this study and is subject to future research.

## 5. Conclusion

The investigation of copper metallizations on silicon substrates that were repeatedly heated with a newly developed laser setup provide the following insights:

- The increase of grain size, related to the applied thermo-mechanical load (thermal cycling) of copper metallizations was investigated. Film A, with a notable incorporation of inorganic species (~100 ppm) revealed a significantly slower grain growth.
- The texture of the tracked regions changes, especially for the fast laser cycled pure Film B, to a pronounced (100)-texture. This is because of growth of grains featuring a preferential orientation in relation to the biaxial tensile/compression stress field within the metallization. Grain rotations are observed too, but do not significantly contribute to texture changes.
- Results are in agreement with investigations using slowly cycled material. The higher the heating/cooling rate, thus the higher the externally applied strain rate, the faster the changes in grain size, RMS roughness and texture occur. This is less evident for the impure Film A.
- The surface topography, quantified by RMS roughness values, shows for both films a linear increase with cycle number.
- The relative increase in sheet resistance is identical for both films, which leads to the assumption that this is due to the increase in film roughness, but not due to the localized formation of voids.
- The laser setup is a very versatile tool for quick screening of thermo-mechanical fatigue of metallizations on silicon substrate. Pieces from wafers can already be used without any further preparation.
- The current experimental setup can easily be adjusted to be used for any other bulk or layered material and even whole devices.

### Acknowledgments

The work was performed in the project EPPL, financially supported by grants from Austria, Germany, The Netherlands, France, Italy, Portugal, and the ENIAC Joint Undertaking (ENIAC JU grant agreement no. 325608). This project is co-funded within the programme "IKT der Zukunft" by the Austrian Ministry for Transport, Innovation and Technology. Support from the company Dr. Mergenthaler GmbH & Co KG (Neu-Ulm, Germany) is gratefully appreciated.

### References

- [1] C.A. Swenson, Recommended Values for the Thermal Expansivity of Silicon from 0 to 1000 K, *J. Phys. Chem. Ref. Data* 12 (1983) 179–182.
- [2] T.A. Hahn, Thermal expansion of copper from 20 to 800 K—standard reference material 736, *J. Appl. Phys.* 41 (1970) 5096–5101, <http://dx.doi.org/10.1063/1.1658614>.
- [3] A.A. Taylor, S.H. Oh, G. Dehm, Microplasticity phenomena in thermomechanically strained nickel thin films, *J. Mater. Sci.* 45 (2010) 3874–3881, <http://dx.doi.org/10.1007/s10853-010-4445-0>.
- [4] W. Heinz, R. Pippa, G. Dehm, Investigation of the fatigue behavior of Al thin films with different microstructure, *Mater. Sci. Eng. A* 527 (2010) 7757–7763, <http://dx.doi.org/10.1016/j.msea.2010.08.046>.
- [5] S. Bigl, S. Wurster, M.J. Cordill, D. Kiener, Advanced Characterization of thermo-mechanical fatigue mechanisms of different copper film systems for wafer metallizations, *Thin Solid Films* 612 (2016) 153–164, <http://dx.doi.org/10.1016/j.tsf.2016.05.044>.
- [6] W. Heinz, W. Robl, G. Dehm, Influence of initial microstructure on thermomechanical fatigue behavior of Cu films on substrates, *Microelectron. Eng.* 137 (2015) 5–10, <http://dx.doi.org/10.1016/j.mee.2014.10.024>.
- [7] W.D. Nix, Mechanical properties of thin films, *Metall. Trans. A* 20 (1989) 2217–2245, <http://dx.doi.org/10.1007/BF02666659>.
- [8] S. Bigl, W. Heinz, M. Kahn, H. Schoenherr, M.J. Cordill, High-temperature characterization of silicon dioxide films with wafer curvature, *JOM* 67 (2015) 2902–2907, <http://dx.doi.org/10.1007/s11837-015-1600-8>.
- [9] M.A. Green, M.J. Keever, Optical properties of intrinsic silicon at 300 K, *Prog. Photovolt. Res. Appl.* 3 (1995) 189–192, <http://dx.doi.org/10.1002/ppa.4670030303>.
- [10] K.L. Chavez, D.W. Hess, A novel method of etching copper oxide using acetic acid, *J. Electrochem. Soc.* 148 (2001) G640–G643, <http://dx.doi.org/10.1149/1.1409400>.
- [11] S. Bigl, S. Wurster, M.J. Cordill, D. Kiener, Site specific microstructural evolution of thermo-mechanically fatigued copper films, *Berg- Huettentechn. Monatsh.* 160 (2015) 235–239, <http://dx.doi.org/10.1007/s00501-015-0355-4>.
- [12] A. Wimmer, M. Smolka, W. Heinz, T. Detzel, W. Robl, C. Motz, et al., Temperature dependent transition of intragranular plastic to intergranular brittle failure in electro-deposited Cu micro-tensile samples, *Mater. Sci. Eng. A* 618 (2014) 398–405, <http://dx.doi.org/10.1016/j.msea.2014.09.029>.
- [13] D. Nečas, P. Klapetek, Gwyddion: an open-source software for SPM data analysis, *Cent. Eur. J. Phys.* 10 (2012) 181–188, <http://dx.doi.org/10.2478/s11534-011-0096-2>.
- [14] F390 - 98, Standard Test Method for Sheet Resistance of Thin Metallic Films with a Collinear Four-Probe Array, 2003.
- [15] CRC Handbook of Chemistry and Physics, 87th ed. Taylor and Francis, 2007.
- [16] P.A. Flinn, D.S. Gardner, W.D. Nix, Measurement and interpretation of stress in aluminum-based metallization as a function of thermal history, *IEEE Trans. Electron Devices* 34 (1987) 689–699.
- [17] M.F. Ashby, H.J. Frost, The Kinetics of Inelastic Deformation above 0 K, in: *Constitutive Equations in Plasticity*, MIT Press, Cambridge, MA, 1975 117–147.
- [18] C.V. Thompson, R. Carel, Texture development in polycrystalline thin films, *Mater. Sci. Eng. B* 32 (1995) 211–219, [http://dx.doi.org/10.1016/0921-5107\(95\)03011-5](http://dx.doi.org/10.1016/0921-5107(95)03011-5).
- [19] P. Sonnweber-Ribic, P. Gruber, G. Dehm, E. Arzt, Texture transition in Cu thin films: electron backscatter diffraction vs. X-ray diffraction, *Acta Mater.* 54 (2006) 3863–3870, <http://dx.doi.org/10.1016/j.actamat.2006.03.057>.